

Limits of nonlinear and dispersive fiber propagation for photonic extreme learning

Andrei V. Ermolaev,¹ Mathilde Hary,^{2,1} Lev Leybov,² Piotr Ryczkowski,²

Anas Skalli,¹ Daniel Brunner,¹ Goëry Genty,² and John M. Dudley^{1,3}

¹*Université Marie et Louis Pasteur, Institut FEMTO-ST,
CNRS UMR 6174, 25000 Besançon, France*

²*Photonics Laboratory, Tampere University, FI-33104 Tampere, Finland*

³*Institut Universitaire de France, Paris, France*

We report a generalized nonlinear Schrödinger equation simulation model of an extreme learning machine based on optical fiber propagation. Using handwritten digit classification as a benchmark, we study how accuracy depends on propagation dynamics, as well as parameters governing spectral encoding, readout, and noise. Test accuracies of over 91% and 93% are found for propagation in the anomalous and normal dispersion regimes respectively. Our simulation results also suggest that quantum noise on the input pulses introduces an intrinsic penalty to ELM performance.

There is currently intense interest in developing photonic hardware capable of performing the computational tasks of artificial intelligence. Often described as optical neuromorphic computing [1, 2], experiments have reported photonic neural networks [3–8], reservoir computers [9–11], and extreme learning machines (ELMs) [7, 12, 13]. One specific area of work has been the application of nonlinear wave propagation directly as a computational resource [14], and recent experiments have reported ELM classification based on nonlinear propagation and supercontinuum generation in optical fiber [15–18]. However, although studies have reported detailed experimental characterization of fiber-based ELM performance over broad parameter ranges [17, 18], guidance from a robust simulation model is clearly needed in order to gain a more complete picture of such nonlinear wave-based computing.

Here we address this question directly using an end-to-end numerical model of nonlinear fiber propagation in an ELM architecture. We analyze performance using the handwritten digit classification benchmark (MNIST dataset, 60,000 training and 10,000 test images), studying how ELM accuracy depends on details of data encoding, propagation dynamics and readout, as well as input pulse noise. Although previous studies have analyzed some parameter dependencies experimentally [17–19], the ability of simulations to explicitly evaluate the effect of quantum and technical noise sources and readily explore different dynamical regimes provides significant new insights.

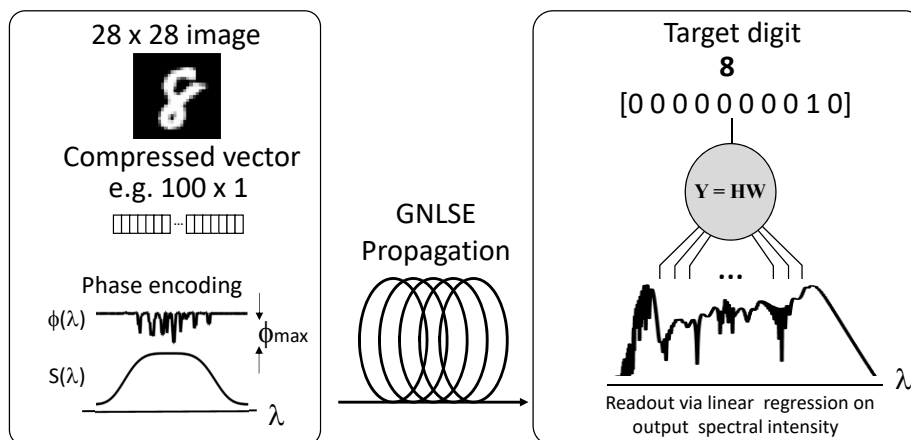


FIG. 1. Schematic of the supercontinuum ELM model showing the three steps of encoding, generalized nonlinear Schrödinger equation (GNLSE) propagation, and spectral readout.

Figure 1 shows the system schematic. An ELM can be considered as a neural network model computing output \mathbf{Y} from input \mathbf{X} . The ELM first projects \mathbf{X} into a higher-dimensional space via a nonlinear transformation $\mathbf{H} = f_{\text{NL}}(\mathbf{X})$, with \mathbf{H} considered as a hidden layer of the system. Based on a training dataset \mathbf{H} (computed from \mathbf{X}) and corresponding target data \mathbf{Y}^T , the ELM

learns a model $\mathbf{Y}^T \approx \mathbf{H}\mathbf{W}^{\text{out}}$. Importantly, \mathbf{W}^{out} can be computed in a single step according to $\mathbf{W}^{\text{out}} \approx \mathbf{H}^\dagger \mathbf{Y}^T$, where \mathbf{H}^\dagger is the Moore–Penrose pseudoinverse of \mathbf{H} . ELMs are computationally extremely efficient because it is only the output weights that are trained through pseudoinverse regression and, in contrast to deep neural networks or reservoir computers, they do not involve backpropagation or dynamical recurrence.

Considering the MNIST digit classification task, for each of the 60,000 training images, we perform: (i) bicubic downsampling and flattening from the 28×28 MNIST image to a length- M vector; (ii) encoding of this vector on the spectral phase (or amplitude) of a femtosecond input pulse; (iii) propagation of the encoded pulse in optical fiber; (iv) readout of the output spectra into K distinct spectral bins after convolution with a Gaussian spectral response function and addition of a detection noise floor. The downsampling step accounts for the limited spectral bandwidth available for encoding on typical input pulses and, consistent with what would be a necessary approach in any practical system, we assume that spectral measurements are made on a single-shot basis with a real-time technique [20]. The underlying physical idea here is that input pulses encoded with different image data will produce distinguishable output spectra after nonlinear propagation. Since output spectra for images corresponding to the same digit (0–9) in the input training set will be expected to exhibit some form of high-dimensional similarity in their structure, a readout step can be trained to identify these similarities and thus classify the corresponding digits.

Specifically, after propagation and readout, the training dataset consists of a $60,000 \times K$ array of spectra. This forms the hidden layer matrix \mathbf{H} , where the propagation dynamics emulate the ELM transformation f_{NL} . The target dataset \mathbf{Y}^T is a $60,000 \times 10$ matrix of the known digits (using a one-hot encoding format), and the $K \times 10$ weight matrix \mathbf{W}^{out} is obtained from solving $\mathbf{W}^{\text{out}} = \mathbf{H}^\dagger \mathbf{Y}^T$ as described above. The model accuracy is determined by applying \mathbf{W}^{out} to \mathbf{H} obtained for 10,000 test images not used in training, and computing the accuracy comparing the ELM predictions and the known test digits. Accuracy associated with the training data is also typically calculated.

Modeling fiber propagation uses the generalized nonlinear Schrödinger equation (GNLSE), written in dimensional form as: $iA_z - 1/2 \beta_2 A_{TT} - i/6 \beta_3 A_{TTT} + 1/24 \beta_4 A_{TTTT} + \gamma(1 + i\omega_0 \partial_T)(A [R * |A|^2]) = 0$ [21]. Here $A(z, T)$ is the complex field envelope (distance z , co-moving time T), the β_k are the dispersion coefficients, γ is the nonlinearity coefficient, and ω_0 is the carrier frequency. The nonlinear response function in the convolution term ($*$) is $R(t) = (1 - f_R)\delta(t) + f_R h_R(t)$, with Raman fraction $f_R = 0.18$ and h_R the experimental Raman response of fused silica [22]. Quantum noise on the input pulse was included via a semiclassical model [22, 23] that has been found to

yield quantitative agreement with experiment in reproducing supercontinuum noise characteristics [24]. Note that we also included a Raman noise source term, but this was found to have negligible influence [22, 24]. For anomalous dispersion regime propagation, we consider dispersion-shifted fiber with 1546.2 nm zero-dispersion wavelength. For a pump wavelength of 1550 nm, parameters are: $\beta_2 = -0.12 \text{ ps}^2 \text{ km}^{-1}$; $\beta_3 = 0.040 \text{ ps}^3 \text{ km}^{-1}$; $\beta_4 = 0 \text{ ps}^4 \text{ km}^{-1}$; $\gamma = 10.7 \text{ W}^{-1} \text{ km}^{-1}$. For normal dispersion regime propagation, we consider dispersion-flattened fiber with parameters at 1550 nm: $\beta_2 = -0.987 \text{ ps}^2 \text{ km}^{-1}$; $\beta_3 = 7.31 \times 10^{-3} \text{ ps}^3 \text{ km}^{-1}$; $\beta_4 = 4.10 \times 10^{-4} \text{ ps}^4 \text{ km}^{-1}$; $\gamma = 7.5 \text{ W}^{-1} \text{ km}^{-1}$. Note that these parameters correspond to commercially-available fiber. It is straightforward to include higher-order dispersion in simulations, but the truncations used here yield the characteristic spectral broadening features of propagation in both dispersion regimes. At the fiber lengths studied, attenuation at the $\sim 0.5\%$ level is neglected. Simulations use a 2^{11} computational grid, but as discussed below, we can analyze the output spectra during readout using different numbers of sampling points.

Images are encoded in the frequency domain on a 30 nm full width at half maximum (FWHM) second-order supergaussian spectrum centered on 1550 nm. The FWHM of the corresponding temporal intensity profile is $\Delta\tau \sim 182 \text{ fs}$ FWHM. For a particular image, the downsampled image vector of length- M is scaled to a desired phase (or amplitude) modulation depth ϕ_{max} . A 30 nm bandwidth allows encoding with 0.3 nm resolution, consistent with commercial Fourier-domain pulse shaping devices. After encoding, we also scale the input pulse to a particular energy at which we wish to study the dynamics.

Figures 2(a) and (b) respectively plot typical anomalous and normal dispersion regime spectral evolution. These results use downsampling to 10×10 ($M = 100$) of one particular image, followed by phase encoding with modulation depth of $\phi_{\text{max}} = 0.25\pi$. The effect of encoding is to add a low-amplitude temporal pedestal at the $\sim -50 \text{ dB}$ level, and for small ϕ_{max} , the corresponding temporal FWHM $\Delta\tau$ is unchanged from that of the unencoded pulse. As a result, it is convenient to scale the input energy so that the pulse injected in the fiber corresponds to a specified parameter $N = (\gamma P_0 T_0^2 / |\beta_2|)^{1/2}$, where timescale $T_0 \approx \Delta\tau / 1.76$. N is a characteristic measure of nonlinear strength which corresponds to soliton number for anomalous dispersion. For anomalous dispersion regime propagation as in Fig. 2(a), an input $N = 10$ corresponds to an energy of 20.7 pJ and peak power of $P_0 = 103 \text{ W}$, and we propagate over 70 m. For normal dispersion regime propagation as in Fig. 2(b), $N = 10$ yields peak power $P_0 = 1215 \text{ W}$ and energy 243 pJ, and we propagate over 40 m. To simulate realistic detection, the output spectra after propagation is convolved with a 1 nm Gaussian spectral response followed by the addition of a -30 dB random noise background

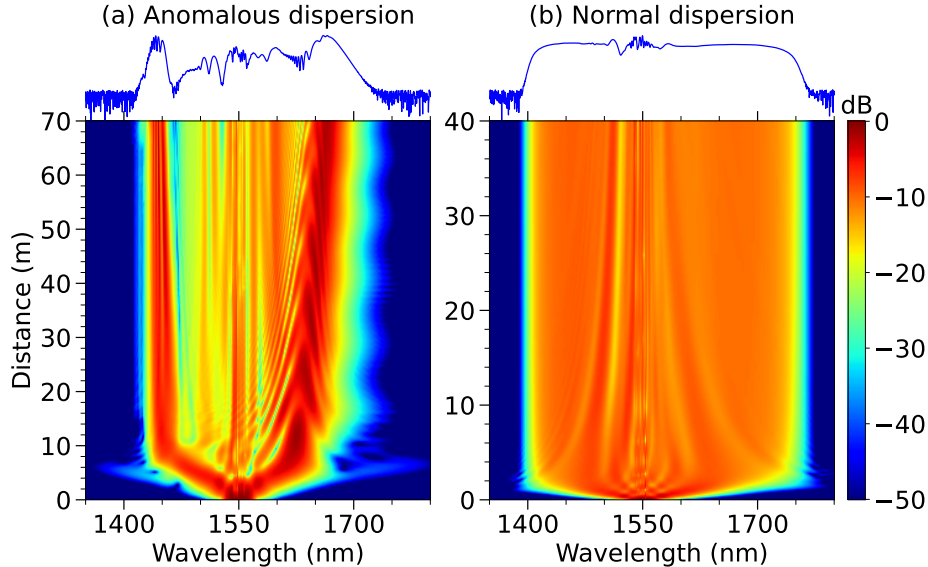


FIG. 2. Simulated spectral evolution of phase-encoded pulses for (a) anomalous and (b) normal dispersion regime dynamics.

to model the finite dynamic range of real-time spectral measurements [20]. The -30 dB level of this constant noise background was computed relative to the peak of the mean spectral intensity of the ensemble. To generate training and testing spectra under different conditions, we define a particular parameter set and then implement these encoding and propagation steps on each of the 70,000 MNIST images.

Figure 3 shows results of this procedure for phase encoding and with anomalous dispersion regime propagation. For downsampling to 10×10 , $\phi_{\max} = 0.25\pi$, and fiber length of 70 m, Fig. 3(a) shows how training (red) and testing (blue) classification accuracy varies as a function of input soliton number N over the range 0.5-13. Figure 3(b) shows similar results for fixed $N = 10$, but with varying fiber length. Test and training results are compared with benchmark linear regression (green dashed line) based on pseudoinverse computation without fiber propagation. These plots show the expected slight decrease in accuracy between training and testing, and also the increase in accuracy exceeding 90% with increasing complexity of propagation at higher N and longer propagation distance. Note that the decrease in accuracy seen in Figs 3(a) and 3(b) around $N = 4$ and 10 m respectively, arises because of localized spectral compression dynamics associated with the early stages of soliton fission at these points.

Figures 3(c) and (d) study aspects of input encoding for $N = 10$ and a fiber length of 70 m. For example, for downsampling to 10×10 , Fig. 3(c) shows how training (red) and testing (blue) accuracy depends on the phase modulation depth ϕ_{\max} . There is a clear optimal value around

$\phi_{\max} \sim 0.25\pi$, and performance away from this point is degraded. Decreasing accuracy for lower modulation depth is expected since image information is weakly encoded and will have limited effect on propagation. The decrease at higher modulation depth arises because greater ϕ_{\max} increasingly modifies the temporal input characteristics, decreasing the peak power at the expense of low amplitude pedestal structure. This results in reduced spectral broadening during propagation. In Fig. 3(d), we apply optimal modulation depth of $\phi_{\max} = 0.25\pi$ and we study how training (red) and testing (blue) accuracies depend on image downsampling i.e. the length M vector describing a $\sqrt{M} \times \sqrt{M}$ image. We clearly see that increasing the image resolution yields improved results, but it is interesting to note that test accuracy approaching 90% can be attained even with only 7×7 downsampling, representing only $\sim 6\%$ of the pixels in the original image.

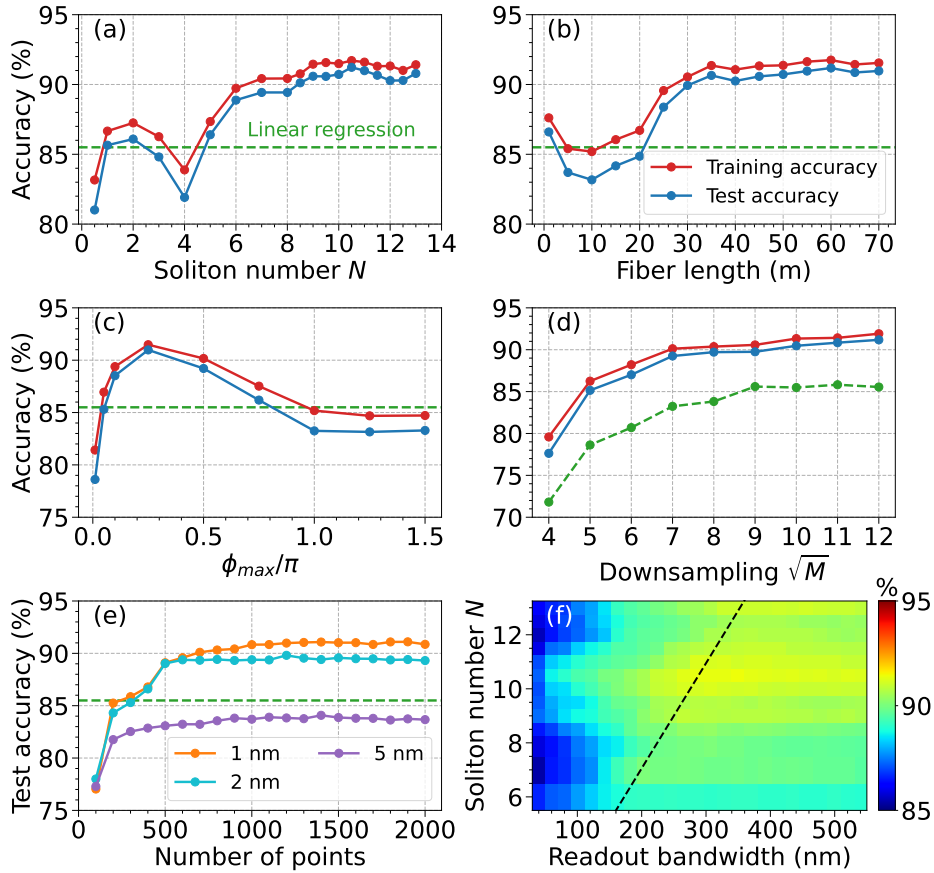


FIG. 3. Results for anomalous dispersion. For downsampling to 10×10 , $\phi_{\max} = 0.25\pi$, and 70 m fiber, training (red) and test (blue) accuracy is shown as a function of (a) soliton number N and (b) fiber length. Green dashed line: linear benchmark. Figures (c-d) use the same color code. For $N = 10$ and 70 m fiber, accuracy is shown: (c) for different ϕ_{\max} , and (d) for input downsampling to $\sqrt{M} \times \sqrt{M}$. (e) Test accuracy varying readout bins and convolution bandwidth as indicated. (f) False color plot of test accuracy dependence on N and readout bandwidth. Dashed line: -20 dB output bandwidth.

The results in Figs 3(a)-(d) base the ELM readout on the full simulated output spectrum (2048 points) over the span 1317-1882 nm, convolved with a 1 nm spectral response and with the addition of -30 dB spectral noise floor. It is of course important to consider how readout parameters influence performance, and these results are shown in Figs 3(e-f). In particular, for downsampling to 10×10 , $\phi_{\max} = 0.25\pi$, and $N = 10$, Fig. 3(e) plots test accuracy reading out the spectrum over the full wavelength span, but changing the readout sampling density using different numbers (100-2000) of equispaced bins. We also compare results considering convolution with three different spectral responses of FWHM: 1 nm (orange), 2 nm (blue), 5 nm (purple). Clearly, more accurate results are seen using a higher sampling density, but it is significant that with 1 nm resolution, $\sim 90\%$ accuracy can be approached with only 700 bins. Figure 3(f) shows related results for the same 10×10 downsampling, $\phi_{\max} = 0.25\pi$, and 1 nm convolution, but here examining how test accuracy depends on the readout bandwidth. The idea is to study whether we need to read out spectral information over the full output bandwidth, or whether a reduced subset of readout wavelengths is sufficient. The false-color plot shows how test accuracy varies with readout bandwidth (centered on 1550 nm) whilst varying N over the range 6-13, where the dashed line shows the corresponding output spectral bandwidth at the -20 dB level. It is clear from the figure that readout over only a portion of the output spectra (i.e. left of the dashed line) leads to reduced accuracy, but once we capture the full output spectral bandwidth i.e. (right of the dashed line) then the accuracy improves (then saturates). This is consistent with the interpretation that nonlinear propagation transforms the encoded image information (initially restricted only to 30 nm around the pump) into the high-dimensional space associated with the broadened spectrum.

Figure 4 shows similar results to those in Figure 3, but for propagation in the normal dispersion regime. The overall trends and dependence on parameters such as N and fiber length are qualitatively alike, although normal dispersion regime propagation consistently shows $\sim 3\%$ quantitative improvement in training and testing accuracy. This can be attributed to the well-known observation of improved noise characteristics in normal dispersion-regime [21]. We note, however, that for both anomalous and normal dispersion, we anticipate that accuracy would ultimately degrade for increased input power and/or fiber length as a result of deleterious effects such as incoherent supercontinuum dynamics, polarization instabilities etc [21].

The studies shown in Figs. 3 and 4 were repeated using spectral amplitude encoding on the input pulses. This involved multiplying the supergaussian input spectrum by an amplitude encoding mask with variable modulation depth. The general trends and results were extremely similar to those obtained with phase encoding in terms of parameter dependence and classification accuracy

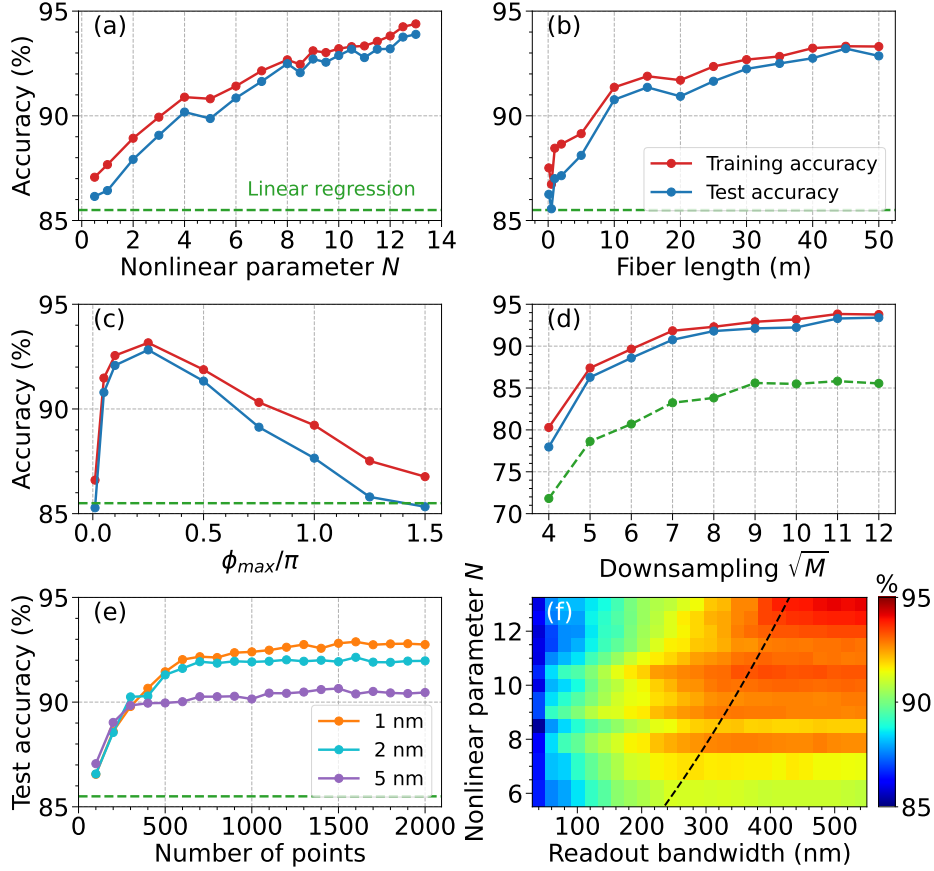


FIG. 4. Results for normal dispersion. For 10×10 downsampling, $\phi_{\max} = 0.25\pi$, and 40 m fiber, training (red) and test (blue) accuracy is shown as a function of (a) nonlinear parameter N and (b) fiber length. Green dashed line: linear benchmark. Figures (c-d) use the same color code. For $N = 10$ and 70 m fiber, accuracy is shown: (c) for different ϕ_{\max} , and (d) for input downsampling to $\sqrt{M} \times \sqrt{M}$. (e) Test accuracy varying readout bins and convolution bandwidth as indicated. (f) False color plot of test accuracy dependence on N and readout bandwidth. Dashed line: -20 dB output bandwidth.

obtained.

In Fig. 5 we plot additional results using phase encoding for $\phi_{\max} = 0.25\pi$ and $N = 10$ studying the impact of noise on ELM performance. Firstly, we recall that the results in Figs. 2-4 were obtained with semiclassical quantum noise on the input pulses and a -30 dB readout noise background. It is straightforward with simulations to model the ELM without input quantum noise or a readout noise floor, and this allows us to study the ideal mathematical properties of the GNLSSE to act as a nonlinear ELM transfer function. These results are shown as the crosses in Fig. 5 and indicate what can be considered upper limit ideal test accuracies of 96.7% and 95.0% for normal and anomalous dispersion regime propagation respectively. Significantly, the addition of only input quantum noise (i.e. again with no imposed readout noise floor) reduces these ideal

test accuracies to 94.8% and 91.9% respectively, an important result that highlights an intrinsic quantum noise penalty for this class of fiber-based ELM. Of course the imposed -30 dB instrumental noise floor on the output spectra reduces accuracy further, with the corresponding results in this case $\sim 93\%$ and $\sim 91\%$ respectively for anomalous and normal dispersion regime propagation.

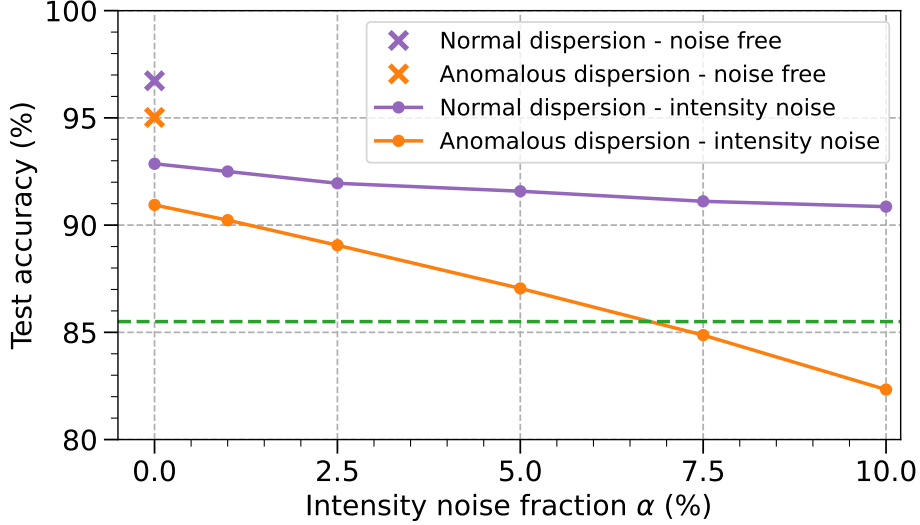


FIG. 5. Lines: Dependence of ELM test accuracy on multiplicative noise for normal (purple) and anomalous (orange) dispersion regime propagation. These results include input quantum noise and a -30 dB readout noise floor. Crosses: ideal accuracies without any input or readout noise. Green dashed line: linear regression benchmark.

As might be expected, any additional noise present on the input pulses has a significant effect on performance. To show this, we apply a simple model for random multiplicative intensity noise of the form $A_{\text{in}}(T) = A_0(T)[1 + \alpha/2\eta(T)]$, where A_0 is the temporal input field after addition of quantum noise and before spectral encoding. Parameter α corresponds to an intensity noise fraction, and $\eta(T)$ is a random variable. Figure 5 shows results applying this noise on input pulses with 10×10 downsampling, phase encoding, $\phi_{\text{max}} = 0.25\pi$ and $N = 10$. It is clear that testing accuracy decreases with increasing noise fraction for both anomalous (orange) and normal (purple) dispersion regime propagation. The results are clearly more degraded in the anomalous dispersion regime, further highlighting the noise sensitivity of anomalous dispersion regime propagation [21].

The GNLSE model framework is clearly a very powerful and flexible tool to fully explore the rich dynamics of nonlinear fiber propagation as applied to ELM systems, and provides important insights for experimental design. Consistent with recent experiments, our results suggest that normal dispersion propagation yields improved accuracy and reduced sensitivity to input noise,

but satisfactory results can still be obtained with anomalous dispersion regime propagation for suitable parameters [15–19]. A further key conclusion is to identify that input pulse quantum noise will likely impose an intrinsic penalty for all nonlinear fiber propagation-based ELMs.

FUNDING

Agence Nationale de la Recherche (ANR-15-IDEX-0003, ANR-17-EURE-0002, ANR-20-CE30-0004); Institut Universitaire de France; ERC Consolidator grant INSPIRE (101044777); Academy of Finland (318082, 320165 Flagship PREIN, 333949).

DISCLOSURES

The authors declare no conflicts of interest.

DATA AVAILABILITY

Data underlying the results presented in this paper may be obtained from the authors upon reasonable request.

-
- [1] D. Psaltis, D. Brady, X.-G. Gu, and S. Lin, *Nature* **343**, 325 (1990).
 - [2] G. Wetzstein, A. Ozcan, S. Gigan, S. Fan, D. Englund, M. Soljačić, C. Denz, D. A. B. Miller, and D. Psaltis, *Nature* **588**, 39 (2020).
 - [3] M. Miscuglio, A. Mehrabian, Z. Hu, S. I. Azzam, J. George, A. V. Kildishev, M. Pelton, and V. J. Sorger, *Opt. Mater. Express* **8**, 3851 (2018).
 - [4] Y. Zuo, B. Li, Y. Zhao, Y. Jiang, Y.-C. Chen, P. Chen, G.-B. Jo, J. Liu, and S. Du, *Optica* **6**, 1132 (2019).
 - [5] A. Jha, C. Huang, and P. R. Prucnal, *Opt. Lett.* **45**, 4819 (2020).
 - [6] J. Liu, Q. Wu, X. Sui, Q. Chen, G. Gu, L. Wang, and S. Li, *Photonix* **2**, 5 (2021).
 - [7] I. Oguz, J.-L. Hsieh, N. U. Dinc, U. Teğın, M. Yildirim, C. Gigli, C. Moser, and D. Psaltis, *Advanced Photonics* **6**, 016002 (2024).
 - [8] N. U. Dinc, I. Oguz, M. Yildirim, C. Moser, and D. Psaltis, *Optical Materials Express* **14**, 2413 (2024).
 - [9] L. Larger, M. C. Soriano, D. Brunner, L. Appeltant, J. M. Gutierrez, L. Pesquera, C. R. Mirasso, and I. Fischer, *Optics Express* **20**, 3241 (2012).
 - [10] F. Dupont, B. Schneider, A. Smerieri, M. Haelterman, and S. Massar, *Optics Express* **20**, 22783 (2012).

- [11] M. Yildirim, I. Oguz, F. Kaufmann, M. R. Escala, R. Grange, D. Psaltis, and C. Moser, *APL Photonics* **8**, 106104 (2023).
- [12] S. Ortín, M. C. Soriano, L. Pesquera, D. Brunner, D. San-Martín, I. Fischer, C. R. Mirasso, and J. M. Gutiérrez, *Scientific Reports* **5**, 14945 (2015).
- [13] U. Teğın, M. Yildirim, I. Oğuz, C. Moser, and D. Psaltis, *Nature Computational Science* **1**, 542–549 (2021).
- [14] G. Marcucci, D. Pierangeli, and C. Conti, *Physical Review Letters* **125**, 093901 (2020).
- [15] B. Fischer, M. Chemnitz, Y. Zhu, N. Perron, P. Roztockı, B. Maclellan, L. Di Lauro, A. Aadhi, C. Rimoldi, T. H. Falk, and R. Morandotti, *Advanced Science* **10**, 2303835 (2023).
- [16] K. F. Lee and M. E. Fermann, *Physical Review A* **109**, 033521 (2024).
- [17] M. Hary, D. Brunner, L. Leybov, P. Ryczkowski, J. M. Dudley, and G. Genty, arXiv:2501.05233 (2025).
- [18] S. Saeed, M. Müftüoğlu, G. R. Cheeran, T. Bocklitz, B. Fischer, and M. Chemnitz, arXiv:2501.18894 (2025).
- [19] I. Muda, A. Maula, and U. Teğın, *Optics Express* **33**, 7852 (2025).
- [20] M. Närhi, L. Salmela, J. Toivonen, C. Billet, J. M. Dudley, and G. Genty, *Nature Communications* **9**, 4923 (2018).
- [21] G. P. Agrawal, *Nonlinear Fiber Optics* (Elsevier, 2019).
- [22] J. M. Dudley, G. Genty, and S. Coen, *Reviews of Modern Physics* **78**, 1135 (2006).
- [23] E. Brainis, D. Amans, and S. Massar, *Physical Review A* **71**, 023808 (2005).
- [24] K. L. Corwin, N. R. Newbury, J. M. Dudley, S. Coen, S. A. Diddams, K. Weber, and R. S. Windeler, *Physical Review Letters* **90**, 113904 (2003).